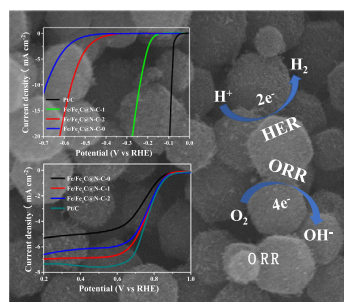# Metal-organic framework derived Fe/Fe₃C@N-doped-carbon porous hierarchical polyhedrons as bifunctional electrocatalysts for hydrogen evolution and oxygen-reduction reactions

Chunsen Song [a], Shikui Wu [a], Xiaoping Shen [a,*], Xuli Miao [a], Zhenyuan Ji [a], Aihua Yuan [b], Keqiang Xu [a], Miaomiao Liu [a], Xulan Xie [a], Lirong Kong [a], Guoxing Zhu [a], Sayyar Ali Shah [a]

[a] School of Chemistry and Chemical Engineering, Jiangsu University, Zhenjiang 212013, PR China
[b] School of Environmental and Chemical Engineering, Jiangsu University of Science and Technology, Zhenjiang 212003, PR China

GRAPHICAL ABSTRACT

ARTICLE INFO

ABSTRACT

The development of simple and cost-effective synthesis methods for electrocatalysts of hydrogen evolution reaction (HER) and oxygen reduction reaction (ORR) is critical to renewable energy technologies. Herein, we report an interesting bifunctional HER and ORR electrocatalyst of Fe/Fe₃C@N-doped-carbon porous hierarchical polyhedrons (Fe/Fe₃C@N-C) by a simple metal-organic framework precursor route. The Fe/Fe₃C@N-C polyhedrons consisting of Fe and Fe₃C nanocrystals enveloped by N-doped carbon shells and accompanying with some carbon nanotubes on the surface were prepared by thermal annealing of $Zn_3[Fe(CN)_6]_2 \cdot xH_2O$ polyhedral particles in nitrogen atmosphere. This material exhibits a large specific surface area of 182.5 m² g⁻¹ and excellent ferromagnetic property. Electrochemical tests indicate that the Fe/Fe₃C@N-C hybrid has apparent HER activity with a relatively low overpotential of 236 mV at the current density of 10 mA cm⁻² and a small Tafel slope of 59.6 mV decade⁻¹. Meanwhile, this material exhibits excellent catalytic activity toward ORR with an onset potential (0.936 V vs. RHE) and half-wave potential (0.804 V vs. RHE) in 0.1 M KOH, which is comparable to commercial 20 wt% Pt/C (0.975 V and 0.820 V), and shows even better stability than the Pt/C. This work provides a new insight to developing multi-functional materials for renewable energy application.

© 2018 Elsevier Inc. All rights reserved.

1. Introduction

The fossil fuel resource crisis and environmental pollution have stimulated the increasing demand for clean and sustainable

* Corresponding author.
  E-mail address: xiaopingshen@163.com (X. Shen).

energy. Hydrogen, the most abundant element on earth, is recognized as the cleanest and ideal fuel. Using H_2 as a power source for fuel cells would be an ideal way to create clean, sustainable energy. Electrocatalytic cathodic water splitting is one of the clean and green ways for the large scale production of pure H_2 gas [1,2]. Therefore, electrochemical water splitting combining with fuel cells could be a good approach to solve the energy and environmental problems. Developing electrocatalytic materials for hydrogen evolution reaction (HER) and oxygen reduction reaction (ORR) become the key requirement for this strategy [3,4]. Currently, the mostly used catalysts for HER and ORR are based on precious metals, such as platinum or platinum-based materials [5–7]. However, their limited reserves and high cost hinder their commercial application. Low cost and earth abundant materials as catalysts for HER and ORR have attracted enormous research interests. In the past decade, many researchers have devoted themselves to explore efficient non-noble-metal HER and ORR catalysts [8–11]. Some carbides [12–14], sulfides [15], phosphides [16], and alloys [17] have been reported as good electrocatalytic materials. Furthermore, the incorporation of these catalysts with carbon materials to construct carbon-based (including nitrogen-doped carbon) hybrids has been demonstrated to be an efficient way to enhance their electrocatalytic activities [18–24]. For instance, MoS_2/reduced graphene oxide (RGO) [18,19], $Fe_{1-x}Co_xS_2$/carbon nanotubes (CNTs) [20], and MoS_x@graphene mesoporous structure/single walled carbon nanotube [21] were reported to show enhanced electrocatalytic performance for HER. Meanwhile, Fe_3C nanoparticles encapsulated in hollow spherical graphitic shells [22], N-doped core shell $N-Fe/Fe_3C@C$ nanostructures [23], and $Fe/Fe_3C@C$ nanoparticles encapsulated in N-doped graphene-CNTs framework [24] performed excellent electrocatalytic activity for ORR. However, the preparation of these electrocatalysts incorporating inorganic nanoparticles with carbon materials usually requires complicated procedures and accurate reaction control. Hence, it is highly desirable to prepare such hybrid electrocatalytic systems by a simple and cost-effective way.

Recently, metal-organic framework (MOF) materials have been used as the precursors/templates for the fabrication of inorganic nanoparticles-carbon hybrid materials [12–14,25–30]. By a simple pyrolysis process, MOF precursors can be transformed into inorganic nanoparticles and carbon materials simultaneously, forming inorganic nanoparticles-carbon hybrids. By this method, various novel hybrids with diverse compositions and rich structures have been fabricated [28–34]. In addition to maintaining the morphology of the MOF precursors, carbon in the hybrids can also be directed to form a variety of interesting structures such as carbon nanotubes (CNTs) and graphene due to the catalysis of the in-situ formed inorganic nanoparticles [35–37]. For example, Zheng et al. synthesized pod-like N-doped CNTs encapsulating FeNi alloy nanoparticles by using $NiFe(CN)_6$ as the precursor, and the obtained materials displayed excellent catalytic performance for ORR and good durability in polymer electrolyte membrane fuel cells [38]. Wu et al. prepared novel nitrogen-doped graphene nanotubes (NGNTs) by annealing the mixture of Co or Fe-MOF and dicyanamide [39,40], and the obtained NGNTs-metal hybrids demonstrated more active sites and could promote charge transfer behavior when used as oxygen reduction electrode materials. Our group prepared FeCo nanocrystals encapsulated in N-doped carbon nanospheres supported on thermal reduced graphene oxide (FeCo-NCNS/TRGO) by annealing $Co_2Fe(CN)_6$ modified graphene oxide, and the as-synthesized materials exhibited excellent catalytic activities towards ORR and the reduction of 4-nitrophenol [41]. These researches demonstrate that the MOF precursor/template method is a simple and effective route to develop novel carbon-based hybrid materials with diverse functions.

Herein, we report the fabrication of an interesting bifunctional electrocatalyst of $Fe/Fe_3C@N$-doped-carbon porous hierarchical polyhedrons ($Fe/Fe_3C@N-C$) by simply pyrolyzing the MOF precursor of $Zn_3[Fe(CN)_6]_2 \cdot xH_2O$ (ZnPBA) in nitrogen atmosphere. The as-prepared $Fe/Fe_3C@N-C$ polyhedrons with a size of *ca.* 800 nm are composed of *ca.* 20 nm $Fe/Fe_3C@N$-doped-carbon core-shell structured nanoparticles, accompanying with some carbon nanotubes on the surface of the polyhedrons. Benefitting from the unique porous hierarchical structure and composition, the $Fe/Fe_3C@N-C$ materials display superior electrocatalytic activity for HER and ORR.

2. Experimental section

2.1. Chemicals

All of the reagents employed in this study are commercially available analytical- grade and used as received without further purification. The water used in the experiment is deionized (DI) water.

2.2. Syntheses

Preparation of $Zn_3[Fe(CN)_6]_2 \cdot xH_2O$ (ZnPBA) polyhedral particles: In a typical synthesis, 500 mg of $K_3Fe(CN)_6$ was dissolved in 500 mL of deionized water to form solution A. 300 mg of $ZnCl_2 \cdot 6H_2O$ and 1 mL of concentrated HCl (37 wt%) were dissolved in 400 mL of deionized water to form solution B. Then the solution B was added into the solution A. The mixed solution was ultrasonicated for 30 min at room temperature and then was aged in the dark for 6 h. The resulted yellow product was collected by centrifugation, washed with deionized water and absolute ethanol for several times, and dried in a vacuum oven at 45 °C for 12 h.

Conversion of the ZnPBA precursor to $Fe/Fe_3C@N-C$ hybrids: The ZnPBA precursor was heated to 800 °C in nitrogen atmosphere with a heating rate of 5 °C min^{-1} and maintained at this temperature for 1 h. After that, the temperature was allowed to cool to room temperature naturally. The product was then collected and denoted as $Fe/Fe_3C@N-C-1$. For comparison, the products obtained with the same procedure but with different holding times of 0 h and 2 h at 800 °C were denoted as $Fe/Fe_3C@N-C-0$ and $Fe/Fe_3C@N-C-2$, respectively.

2.3. Characterization of the electrocatalysts

The phase structure of the as-synthesized samples was characterized by powder X-ray diffraction (XRD, Rigaku D/MAX 2400) using Cu-K_α radiation (λ = 1.5406 Å) at a scanning rate of 5° min^{-1}. The morphology, size and microstructure of the products were examined by scanning electron microscopy (SEM, JSM-6480) and transmission electron microscopy (TEM, JEM-2100). The composition of the product was estimated by energy-dispersive X-ray spectrometry (EDX attached to SEM). Elemental mapping images were acquired on a Tecnai G2 F30 S-Twin TEM. Raman scattering was performed on a DXR Raman spectrometer using a 532 nm laser source. X-ray photoelectron spectroscopy (XPS) measurements were done by using a Thermo ESCALAB 250XI spectrometer with a monochromic Al K_α source (1486.6 eV, voltage of 15 kV, emission current of 10 mA). Thermogravimetric (TG) analysis was conducted on an integrated thermal analyzer (NETZSCH STA449C) at a heating rate of 5 °C min^{-1} in nitrogen atmosphere. The magnetic measurements were performed using a vibrating sample magnetometer (VSM, Nanjing University HH-15) at room temperature (300 K). Brunauer-Emmett-Teller (BET) surface area was collected at 77 K using a Micromeritics ASAP 2020 apparatus and porosity analyzer.

2.4. Electrochemical measurements

The catalytic activities of the as-prepared hybrids toward HER were conducted on a typical three-electrode set-up using a CHI 760 D electrochemical analyzer (ChenHua Instruments, Shanghai, China) at room temperature. Saturated calomel electrode (SCE) and Pt foil were used as the reference and counter electrodes, respectively. Glassy carbon electrodes (GCE, 3 mm in diameter) coated with the as-prepared samples were used as the working electrodes. For the fabrication of working electrode, the catalyst ink was prepared by dispersing 5.0 mg of catalyst into a mixed solvent containing 0.98 mL of absolute ethanol and 20 μL of 5 wt% Nafion solution followed with sonication for about 30 min to form a homogeneous ink. Prior to the surface coating, the GCE was polished using 0.05 μm alumina powder, followed by sonication in absolute ethanol, and then allowed to dry at room temperature. Then 5 μL of the catalyst ink was loaded onto GCE and dried at room temperature naturally. Before the electrochemical measurement, the electrolyte (0.5 M H_2SO_4) was degassed by bubbling nitrogen for about 10 min. Linear sweep voltammetry (LSV) was then conducted at the scan rate of 5 mV s^{-1}. Electrochemical impedance spectra (EIS) were measured in 0.1 M KCl solution containing 2.5 mM $K_3[Fe(CN)_6]$/$K_4[Fe(CN)_6]$ (1:1) with a sinusoidal ac perturbation of 5 mV over a frequency range of 100 kHz to 100 mHz. To collect the H_2 generated from the cathode in 0.5 M H_2SO_4, a constant potential of -0.3 V was adjusted for 3 h. The evoluted H_2 was monitored every 30 min by a gas chromatography (Agilent, GC7920).

The catalytic activities of the as-prepared hybrids toward ORR were conducted on a typical three-electrode set-up using a CHI 760 D electrochemical analyzer (ChenHua Instruments, Shanghai, China) in a 0.1 M KOH aqueous solution. Ag/AgCl and Pt foil were used as the reference and counter electrodes, respectively. A rotating-ring disk electrode (RRDE) with a glassy carbon disk (5 mm in diameter) and gold ring was used as the working electrodes. For the fabrication of working electrode, the catalyst ink was prepared by dispersing 10.0 mg of catalyst into a mixed solvent containing 1.0 mL of absolute isopropyl alcohol and 60 μL of 5 wt% Nafion solution followed with sonication for about 30 min to form a homogeneous ink. 10 μL of the catalyst ink was loaded onto the surface of the glassy carbon disk and dried at room temperature naturally. Prior to the measurement, the electrolyte (0.1 M KOH) was deaerated by nitrogen or oxygen for about 30 min. The CV scanning potentials started from 0.2 V to -1 V (vs. Ag/AgCl) at a sweep rate of 50 mV s^{-1} in N_2 or O_2-saturated electrolyte. For the LSV measurements, the ring potential was held constant at 0.286 V (vs. Ag/AgCl). The LSV curves were recorded in the potential range of 0.2 to -1 V (vs. Ag/AgCl) with 10 mV s^{-1} over rotation speeds of 625, 1225, 1600, 2025 rpm in O_2-saturated electrolyte. The electron transfer number (n) at various electrode potentials was calculated on the basis of the Koutecky-Levich equation [42]:

$$\frac{1}{j} = \frac{1}{j_L} + \frac{1}{j_K} = \frac{1}{B\omega^{1/2}} + \frac{1}{j_K} \quad (1)$$

$$B = 0.62nFC_o(D_o)^{2/3}v^{-1/6} \quad (2)$$

where j is the measured current density, j_K and j_L are the kinetic- and diffusion limiting current densities, ω is the angular velocity, F is the Faraday constant, C_o is the bulk concentration of O_2, D_o is the diffusion coefficient of O_2, and v is the kinematic viscosity of the electrolyte.

In addition, based on the RRDE measurements, the transferred electron number per oxygen molecule (n) and H_2O_2% were also calculated by the followed equations:

$$n = 4\frac{I_d}{I_d + I_r/N} \quad (3)$$

$$H_2O_2\% = 200\frac{I_r/N}{I_d + I_r/N} \quad (4)$$

where I_d is the disk current and I_r the ring current, and N is the current collection efficiency of the Pt ring, which was determined to be 37%. The potentials were referenced to a reversible hydrogen electrode (RHE).

3. Results and discussion

3.1. Characterization of the as-prepared samples

The ZnPBA precursor was synthesized by reacting $K_3Fe(CN)_6$ with $ZnCl_2$, and the as-prepared sample was characterized by XRD, SEM and TG analysis. It can be seen from the XRD pattern (Fig. 1a) that all of the diffraction peaks can be assigned to the cubic phase $Zn_3[Fe(CN)_6]_2·xH_2O$ (JCPDS, No. 38-0687). The SEM images (Fig. S1a and S1b) reveal that the precursor is composed of polyhedral particles with a size of $ca.$1.0 μm. The TG analysis of the precursor exhibits two obvious weight loss stages (Fig. S2a). The weight loss below 100 °C can be ascribed to the loss of crystal water and adsorbed water molecules in $Zn_3[Fe(CN)_6]_2·xH_2O$. The weight loss at $ca.$ 300–600 °C can be attributed to the decomposition of the cyanide-metal framework. After 650 °C, the continuous weight loss can be ascribed to the evaporation of the generated Zn in the inert atmosphere.

Fig. 1b presents the XRD pattern of the as-prepared Fe/Fe₃C@N-C-1. It displays a wide diffraction peak at 2θ of about 25° (inset of Fig. 1b), which can be attributed to the (0 0 2) reflection of graphitic carbon [35,43], demonstrating that carbon species is formed in the pyrolysis process. The weak and wide (0 0 2) peak suggests the few layer numbers of the graphitic carbon. The peaks at 2θ of 37.8°, 40.5°, 42.8°, 43.7°, 44.6°, 45.0°, 49.1° and 51.8° can be indexed into (1 2 1), (2 0 1), (2 1 1), (1 0 2), (2 2 0), (0 3 1), (2 2 1) and (1 2 2) planes of Fe₃C (JCPDS, No. 89-2867), respectivelty. The peaks at 2θ of 44.7° and 65.0° can be ascribed to α-Fe (JCPDS, No. 87-0722). No other peaks from impurity can be observed. The XRD result indicates that the hybrid is composed of graphite carbon, Fe and Fe₃C.

The typical SEM images of the as-prepared Fe/Fe₃C@N-C-1 are shown in Fig. 2a and 2b. Well-defined polyhedral particles with an average diameter of $ca.$ 800 nm can be clearly observed, indicating that the original polyhedral morphology of the precursor was well kept after the annealing. However, the surface of the polyhedrons became rough, and was covered by some fluffy substance (Fig. 2b). TEM images provide more details of the morphology and microstructure. As shown in Fig. 2c and d, the polyhedrons consist of a large number of tiny nanoparticles with a size of $ca.$ 20 nm, and a clear porous structure can be found around the nanoparticles. On the surface of the polyhedrons, some CNTs can be observed. The nanoparticles at the tips of CNTs suggest the tip growth mechanism of these tubes [35]. During the high temperature annealing process, the Fe^{III} species was reduced to metal Fe particles, and simultaneously the cyanogroups (CN⁻) were decomposed, releasing a large amount of carbon nitride gases, which could be captured by the Fe particles to catalyze the growth of CNTs [35]. The high resolution TEM (HRTEM) image (Fig. 2e) reveals that the nanoparticle composing the polyhedron has a core-shell structure, in which the shell consists of well-ordered layers with a lattice spacing of about 0.34 nm, corresponding to the (0 0 2) planes of graphitic carbon, while the lattice spacing of 0.21 nm in the core matches well with that of (2 1 0) planes of orthorhombic Fe₃C (0.2102 nm). According to EDX analysis
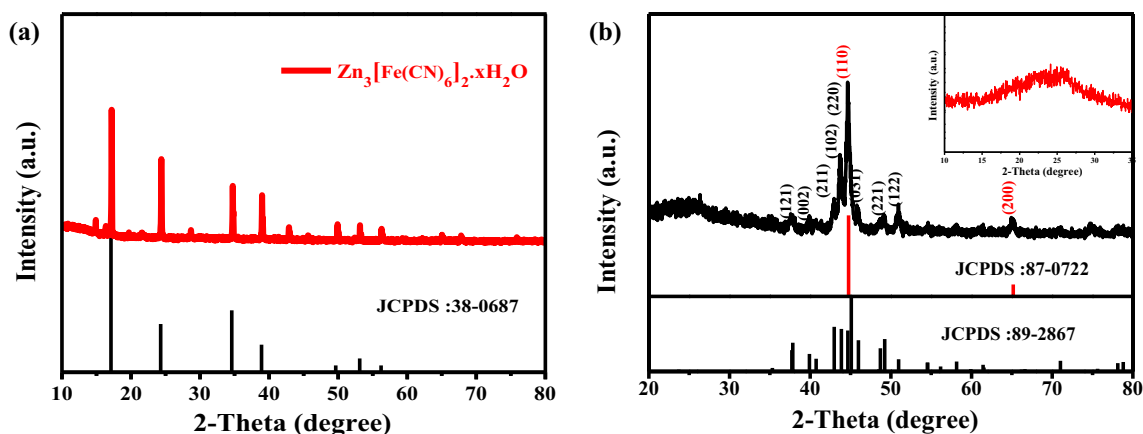
Fig. 1. XRD patterns of (a) the as-prepared ZnPBA polyhedrons and (b) Fe/Fe₃C@N-C. The inset in (b) is the local magnified image.
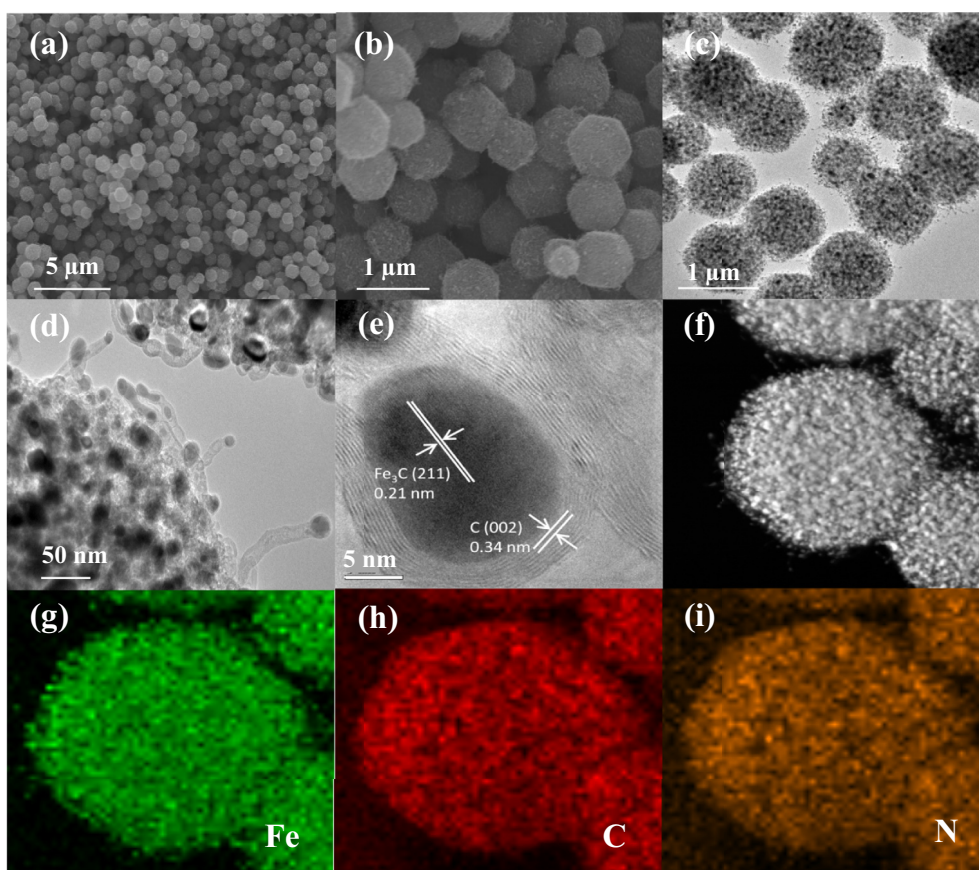

Fig. 2. (a, b) SEM, (c, d) TEM, (e) HRTEM, and (f–i) the elemental mapping images of the as-prepared Fe/Fe₃C@N-C-1.

(Fig. S3), the weight percent contents of Fe, C and N in the hybrid are about 71.17% , 27.12% and 1.61%, respectively. The presence of the element N verifies the formation of N-doped carbon layers. The distribution of Fe, C and N elements was determined by the elemental mapping. As shown in Fig. 2f–i, the distribution of Fe, C and N elements in the polyhedral particles is highly homogeneous. The above results demonstrate that the Fe/Fe₃C@N-C hybrid with well-defined polyhedron morphology and interesting porous hierarchical structure has been successfully prepared by the simple and versatile MOF precursor route.

XPS technique was also used to characterize the elemental composition and chemical states of Fe/Fe₃C@N-C. The survey spectrum in Fig. 3a confirmed the presence of Fe, C and N elements in Fe/Fe₃-C@N-C. The high-resolution spectrum of Fe 2p (Fig. 3b) shows four distinct peaks at 707.8, 710.7, 720.1, 724.3 eV, corresponding to the Fe^0 $2p_{3/2}$, Fe^{III} $2p_{3/2}$, Fe^0 $2p_{1/2}$ and Fe^{III} $2p_{3/2}$, respectively, suggesting the existence of Fe and Fe₃C [24]. What's more, according to previous reports [14,44], the peak at 710.7 eV suggests that Fe is present as N coordinated Fe (Fe-N_x) in the Fe/Fe₃C@N-C sample. The C1s spectrum (Fig. 3c) can be deconvoluted into C—C/C═C (284.8 eV) and C—N (285.4 eV) peaks. As shown in Fig. 3d, the N1s spectrum can be deconvoluted into three peaks: pyridinic N (398.4 eV), pyrrolic N (400.0 eV) and graphitic N (401.1 eV), which is consistent with the related materials reported previously [45–47].
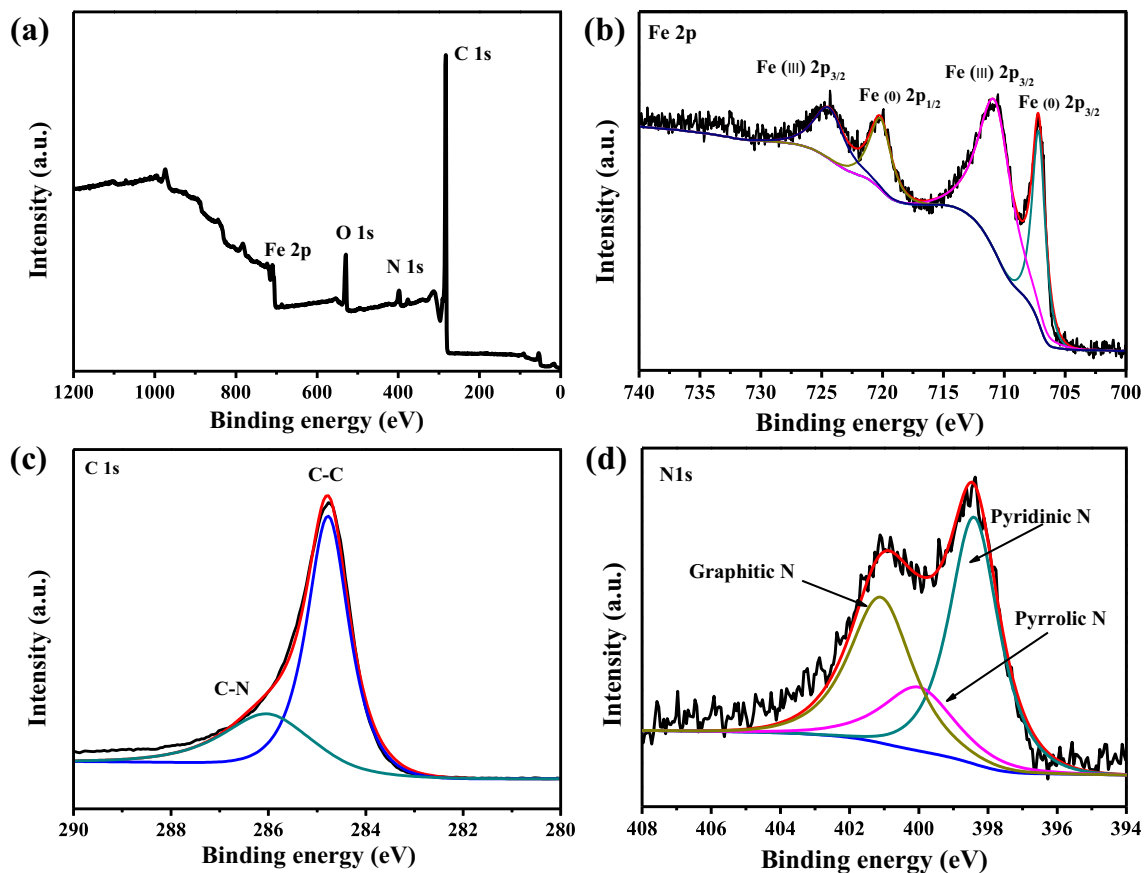
Fig. 3. XPS spectra of the as-prepared Fe/Fe$_3$C@N-C-1: (a) survey, (b) Fe 2p, (c) C 1s, (d) N 1s.

To further study the role of N species in the electrocatalytic reactions, the samples of Fe/Fe$_3$C@N-C-0 and Fe/Fe$_3$C@N-C-2 were also analyzed by XPS. As shown Fig. S4, the N 1s spectra of them could be deconvoluted to pyridinic-N, pyrrolic-N and graphitic N. The proportions of the different N species can be obtained based on the peak areas, and the data are listed in Table 1. It can be seen that the proportion of pyridinic-N in Fe/Fe$_3$C@N-C-1 is 48%, which is the largest among these three samples. Since pyridinic N could largely favor mass and charge transfer, as well as the electrochemical reaction [48]. A high proportion of pyridinic N would lead to high electrocatalytic activity for ORR and HER [14,49]. In addition, it should be noted that N-containing species in these samples are capable of coordinating with Fe to form Fe-N$_x$ moieties, which could serve as electrochemically active sites to enhance the electrocatalytic activity [44,46]. Therefore, a high content of pyridinic N together with highly dispersed Fe-N$_x$ active sites in Fe/Fe$_3$C@N-C-1 is expected to enhance the intrinsic catalytic activity.

The effect of annealing time on the products was also investigated. As shown in Fig. S5, the Fe/Fe$_3$C@N-C-0 synthesized without holding time at 800 °C exhibits well-defined polyhedral morphology but with less CNTs on the surface (Fig. S5a and S5b), whereas Fe/Fe$_3$C@N-C-2 with 2 h holding time shows less regular shape

with some tubular bulges on the surface, and some of the polyhedrons were destroyed (Fig. S5c and S5d). Contrast to Fe/Fe$_3$C@N-C-0 and Fe/Fe$_3$C@N-C-2, the Fe/Fe$_3$C@N-C-1 shows not only well-defined polyhedral morphology, but also possesses plenty of CNTs on the surface of the polyhedrons. Therefore, the annealing time has an important influence on the morphology and microstructure of the Fe/Fe$_3$C@N-C products.

Raman spectroscopy is a widely used tool for characterizing detailed structural feature of carbon-based materials. The typical Raman spectra of the Fe/Fe$_3$C@N-C-1, Fe/Fe$_3$C@N-C-0, and Fe/Fe$_3$C@N-C-2 hybrids are shown in Fig. S2b. All the spectra show two dominant peaks at about 1351 and 1586 cm^{-1}, which are ascribed to the D and G bands of the defected graphitic materials, respectively [50–53]. The intensity ratio (I_D/I_G) of the D to G bands decreases in the order of Fe/Fe$_3$C@N-C-0, Fe/Fe$_3$C@N-C-1, and Fe/Fe$_3$C@N-C-2, suggesting that the degree of graphitization increases with the increasing annealing time. The relatively strong D bands in these samples mean the formation of plenty of structural defects or microstructural rearrangement due to the presence of nitrogen doping in the carbon matrix [54,55].

The porosity and specific surface area of the as-prepared Fe/Fe$_3$-C@N-C samples were further investigated by Brunauer-Emmett-

Table 1
The contents of doped-N and the relative ratios of different N species.

Catalyst	N (at%)	Pyridinic N (%)	Pyrrolic N (%)	Graphitic N (%)
Fe/Fe$_3$C@N-C-0	7.18	31	20	49
Fe/Fe$_3$C@N-C-1	7.03	48	17	35
Fe/Fe$_3$C@N-C-2	6.64	37	23	40

Teller (BET) measurement. As shown in Fig. 4a–c, these samples show the type IV N_2 adsorption/desorption isotherms, suggesting the formation of mesoporous structures [56]. The BET surface areas are 63.8, 182.5 and 118.6 $m^2 g^{-1}$ for Fe/Fe$_3$C@N-C-0, Fe/Fe$_3$C@N-C-1 and Fe/Fe$_3$C@N-C-2, respectively, and the corresponding pore volumes were about 0.388, 0.788 and 0.633 $cm^3 g^{-1}$, respectively. The average pore sizes of Fe/Fe$_3$C@N-C-0, Fe/Fe$_3$C@N-C-1 and Fe/Fe$_3$C@N-C-2 are 3.56, 3.81 and 3.81 nm, respectively. The Fe/Fe$_3$C@N-C-1 with the highest surface area and the largest pore volume is anticipated to facilitate mass transfer resulting in rapid reaction kinetics and providing more active sites to promote the electrocatalytic energy conversion activities.

The magnetic properties of Fe/Fe$_3$C@N-C-0, Fe/Fe$_3$C@N-C-1 and Fe/Fe$_3$C@N-C-2 samples are shown in Fig. 4d. The saturation magnetization intensity (M_s) of the three samples is 36.77, 67.01 and 65.68 emu g^{-1}, respectively. And the coercive force (H_c) is 12.85, 21.74 and 18.68 Oe, respectively. These results indicate that the Fe/Fe$_3$C@N-C materials possess excellent ferromagnetic properties, and the annealing time has an obvious effect on their magnetic properties.

The formation process of the Fe/Fe$_3$C@N-C hierarchical structures can be briefly described as follows. When the precursor was heated under the nitrogen atmosphere, the Fe—C—N—Zn bonds broke. The CN^- groups decomposed to produce nitrogen and carbon species. The Fe atoms formed metal Fe nanoparticles, which reacted partly with carbon species to generate Fe$_3$C. The nitrogen and carbon species formed nitrogen-doped carbon layers on the surface of the as-formed Fe$_3$C nanoparticles, resulting in Fe/Fe$_3$C@N-C core-shell nanostructure. Meanwhile, some carbon nanotubes were grown on the surface of the polyhedrons due to the catalysis of metal Fe. Under the high temperature, Zn species was evaporated to lead to porous structure. The polyhedron morphology of the precursor could be well retained through adjusting the annealing condition. As a result, the Fe/Fe$_3$C@N-C porous

hierarchical structure with well-defined polyhedron morphology was obtained.

3.2. Electrocatalytic activities toward HER and ORR

Considering the interesting structure and composition, the as-prepared Fe/Fe$_3$C@N-C hybrids were investigated as the electrocatalysts for HER and ORR. The HER activities of Fe/Fe$_3$C@N-C-0, Fe/Fe$_3$C@N-C-1 and Fe/Fe$_3$C@N-C-2 were measured in 0.5 M H_2SO_4 solution using a typical three-electrode system. For comparison, the electrochemical performance of commercial Pt/C (20 wt%) electrode was also investigated under the same condition. Fig. 5a presents the LSV polarization curves. Among all the tested samples, the Pt/C electrode shows the lowest overpotential, indicating the highest electrocatalytic activity for HER [57]. Compared with Fe/Fe$_3$C@N-C-0 and Fe/Fe$_3$C@N-C-2 electrodes, Fe/Fe$_3$C@N-C-1 electrode exhibits a smaller overpotential of 236 mV at the current density of 10 mA cm^{-2}, and achieves a larger current density of 20 mA cm^{-2} at the overpotential of 260 mV. This directly reflects the highest electrocatalytic efficiency of Fe/Fe$_3$C@N-C-1 among the three Fe/Fe$_3$C@N-C products.

As shown in Fig. 5b, the linear regions of the Tafel plots are fitted well to the Tafel equation ($\eta = b \log j + a$, where b is the Tafel slope and j is the current density). The parameters about the HER activity derived from the Tafel plots are summarized in Table S1. It can be seen that the Fe/Fe$_3$C@N-C-1 electrode exhibits a small Tafel slope of 59.6 mV decade^{-1}, which is much smaller than that of Fe/Fe$_3$C@N-C-0 (148.3 mV decade^{-1}) and Fe/Fe$_3$C@N-C-2 (113.2 mV decade^{-1}), confirming the better electrocatalytic activity of Fe/Fe$_3$C@N-C-1. The exchange current density (j_0) for the Fe/Fe$_3$C@N-C-1 electrocatalyst is ca. 5.8×10^{-2} mA cm^{-2}, which is higher than that of Fe/Fe$_3$C@N-C-0 (2.8×10^{-2} mA cm^{-2}) and Fe/Fe$_3$C@N-C-2 (3.98×10^{-2} mA cm^{-2}). The larger j_0 value further reveals the superior electrocatalytic activity of Fe/Fe$_3$C@N-C-1
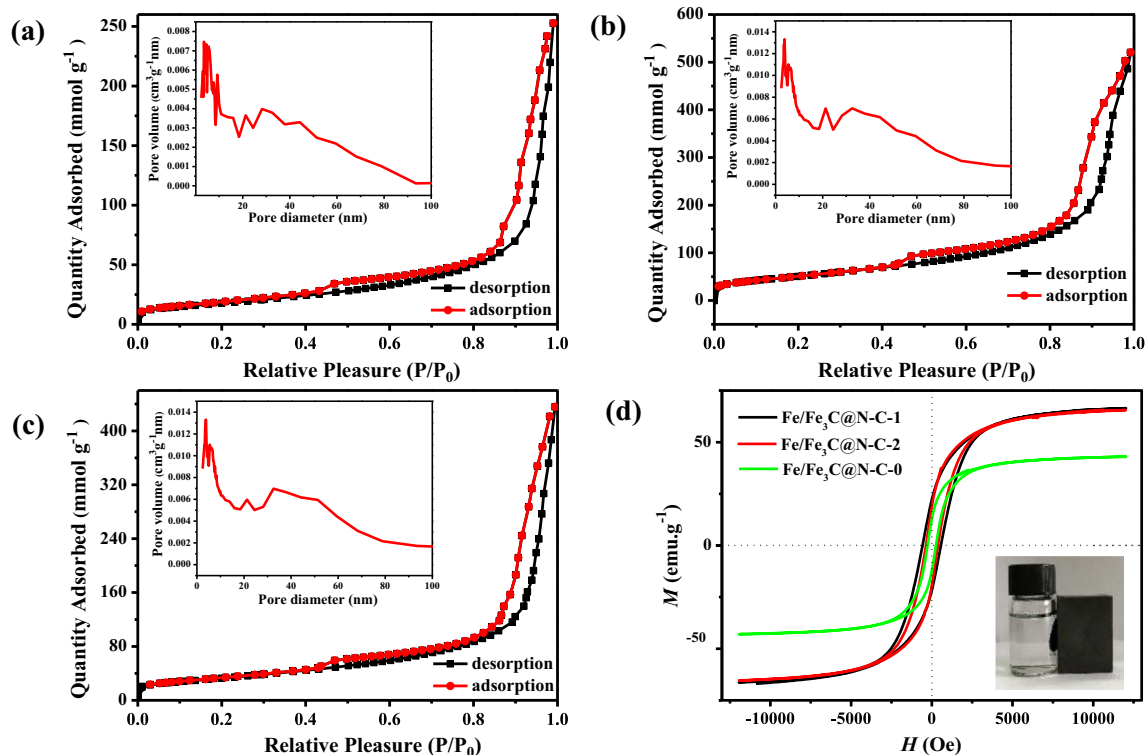

Fig. 4. (a, b, c) Nitrogen adsorption and desorption isotherms (inset is the pore size distribution curves), and (d) magnetic hysteresis loops of Fe/Fe$_3$C@N-C-0, Fe/Fe$_3$C@N-C-1 and Fe/Fe$_3$C@N-C-2.
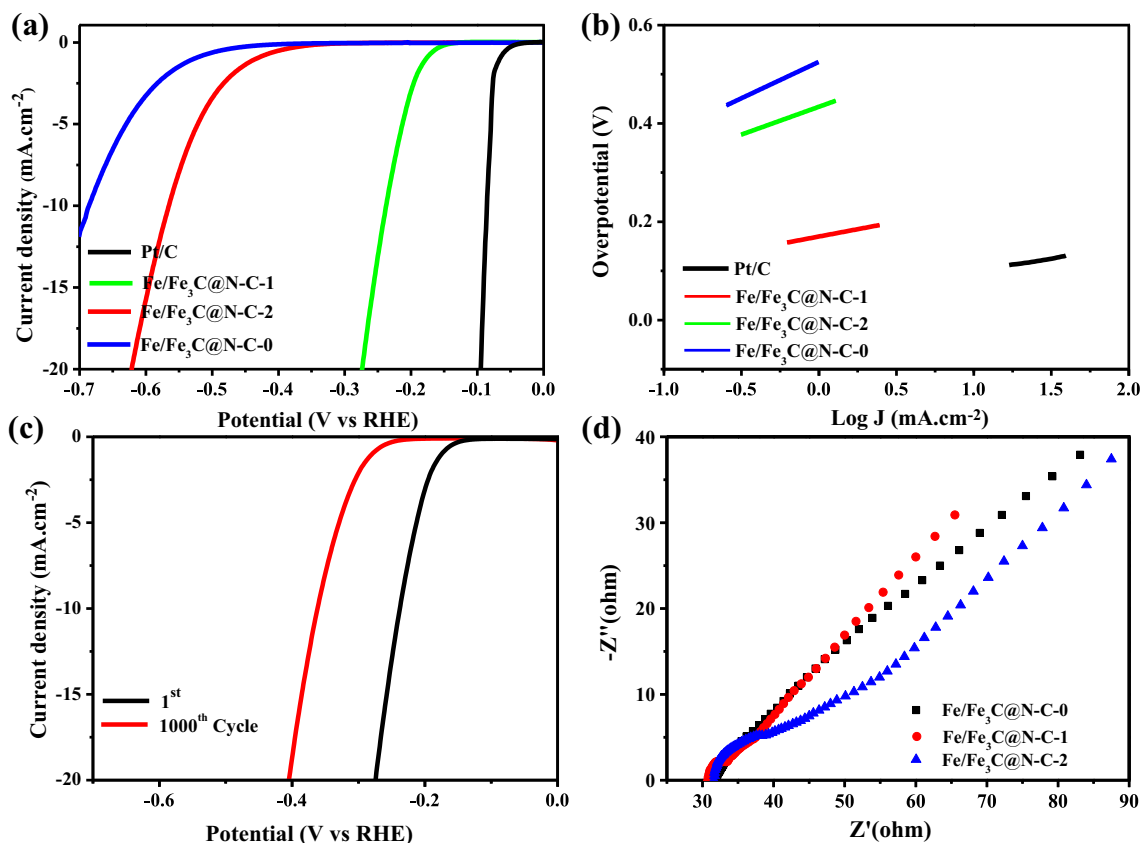
Fig. 5. (a) LSV polarization curves and (b) the corresponding Tafel plots; (c) LSV polarization curves of Fe/Fe₃C@N-C-1 electrode at the 1st and the 1000th cycle; (d) Nyquist plots of Fe/Fe₃C@N-C-0, Fe/Fe₃C@N-C-1 and Fe/Fe₃C@N-C-2.

compared to Fe/Fe₃C@N-C-0 and Fe/Fe₃C@N-C-2 (Fig. S6). In order to investigate the electrocatalytic stability of Fe/Fe₃C@N-C-1 for HER, the LSV polarization measurements of Fe/Fe₃C@N-C-1 electrode were repeated for 1000 cycles in 0.5 M H_2SO_4 solution. As shown in Fig. 5c, the catalytic performance of the electrode shows a noticeable decrease after 1000 cycles, probably due to the dissolution of Fe and Fe₃C in the acid solution [58,59]. Furthermore, the Faradaic efficiency of as-prepared Fe/Fe₃C@N-C-1 was probed by comparing the volume of generated gas and the quantity of charges passed the Fe/Fe₃C@N-C-1 electrode in a potentiostatic electrolysis measurement carried out at an overpotential of −0.3 V for 3 h (Fig. S7a). As shown in Fig. S7b, the measured points nearly overlap the calculated curve, which meant the Faradaic efficiency is nearly 100%, suggesting the potential application of Fe/Fe₃C@N-C-1 in HER.

To understand the electrochemical characteristic of the electrode materials, the electrochemical impedance spectrum (EIS) was used to investigate the cathodes of the Fe/Fe₃C@N-C-0, Fe/Fe₃C@N-C-1 and Fe/Fe₃C@N-C-2 at their corresponding open circuit voltage with an amplitude of 5 mV in the frequency range of 100 kHz to 0.1 Hz. The Nyquist plots are shown in Fig. 5d. The semicircle part at the high frequency region is associated with the charge-transfer process at the electrode interface, and a smaller radius implies more efficient charge transfer. Consequently, the smaller arc of Fe/Fe₃C@N-C-1 compared to Fe/Fe₃C@N-C-0 and Fe/Fe₃C@N-C-2 implies that the increased electron conductivity of the electrode and improved charge transfer efficiency at the electrode interface, which could contribute to the better electrochemical performance of Fe/Fe₃C@N-C-1.

The potential application of the as-prepared Fe/Fe₃C@N-C catalysts for ORR was also investigated. The catalytic activities for ORR were assessed using rotating ring-disk electrode (RRDE) in 0.1 M

KOH solution saturated with O_2 and compared with commercial 20 wt% Pt/C catalyst. As shown in Fig. 6a, the CV curve for Fe/Fe₃C@N-C-1 displays a prominent cathodic peak at 0.759 V (vs. RHE) in O_2-saturated solution, which is not observed in the N_2-saturated solution, suggesting the catalytic reduction of dissolved O_2. The LSV polarization curves of the Fe/Fe₃C@N-C catalysts and commercial Pt/C were measured at a rotation rate of 1600 rpm. As shown in Fig. 6b, Fe/Fe₃C@N-C-1 shows better catalytic activity than the Fe/Fe₃C@N-C-0 and Fe/Fe₃C@N-C-2 catalysts. The onset potential (E_{onset}) and half-potential ($E_{1/2}$) of Fe/Fe₃C@N-C-1 are 0.936 V and 0.804 V (vs. RHE), which is higher than those of Fe/Fe₃C@N-C-0 (0.896 V and 0.778 V vs. RHE) and Fe/Fe₃C@N-C-2 (0.920 V and 0.781 V vs. RHE) and almost comparable to those of commercial Pt/C (0.975 V and 0.820 V vs. RHE) (Table S2). The catalytic performance of the as-prepared Fe/Fe₃C@N-C-1 was also compared with those of Fe₃C based catalysts reported previously. As shown in Table S3, the ORR activity of Fe/Fe₃C@N-C-1 is superior or comparable to previous reports. Through comparing the catalytic activities of the Fe/Fe₃C@N-C catalysts, it was found that ORR and HER catalytic activities of these catalysts are correlated with the contents of pyridinic N species in them. As shown above, the electrocatalytic activities of the Fe/Fe₃C@N-C hybrids increase with the increasing content of pyridinic N. Therefore, it can be inferred that pyridinic N plays an important role in giving rise to more active sites and contributing to boosting the electrocatalytic activity [60,61].

Fig. 6c shows the ORR polarization curves of Fe/Fe₃C@N-C-1 under different rotation rates. The current densities increase with the increasing rotation rates. The nearly parallel Koutecky-Levich (K-L) plots (Inset of Fig. 6c) demonstrate a good linear relationship between j^{-1} and $\omega^{-1/2}$ from 0.45 to 0.60 V vs. RHE, implying first-order reaction kinetics with respect to O_2 concentration. The
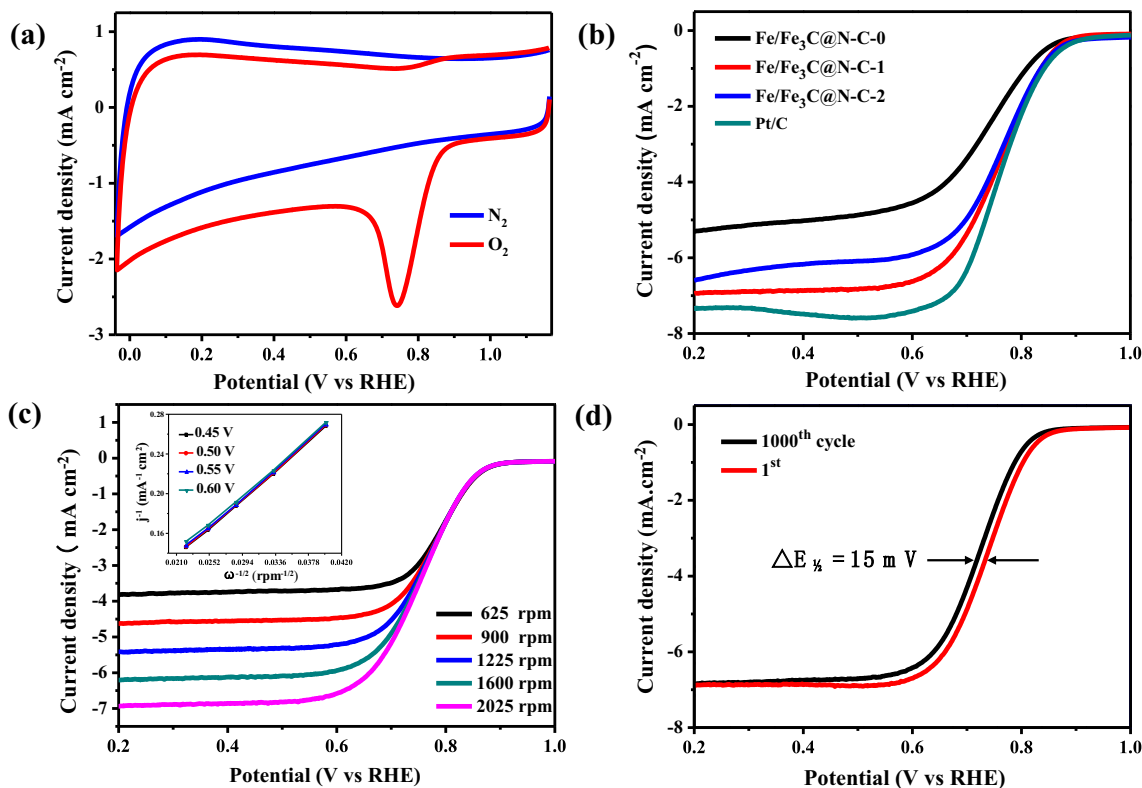
Fig. 6. (a) Cyclic voltammetry of Fe/Fe₃C@N-C-1 in O₂ or N₂-saturated 0.1 M KOH; (b) ORR polarization curves of different catalysts for the ORR activity at 1600 rpm, (c) ORR polarization curves of Fe/Fe₃C@N-C-1 at different rotating speeds (inset is the corresponding *K-L* plots at different potentials), (d) ORR polarization curves of Fe/Fe₃C@N-C-1 at the 1st and the 1000th cycle in O₂-saturated 0.1 M KOH at 1600 rpm.

electron transfer number (n) for Fe/Fe₃C@N-C-1 catalyst calculated from K-L equation are 4.08–4.15, approaching the ideal value of 4.0, confirming a four-electron dominated ORR pathway. The long-term stability of Fe/Fe₃C@N-C-1 was evaluated by 1000 consecutive CV cycles in O₂-saturated 0.1 M KOH by cycling the potential between −1.0 V and 0.2 V (*vs.* Ag/AgCl) at a scan rate of 50 mV s^{-1} (Fig. 6d). Comparing the polarization curves before and after 1000 cycles, there is only a minor negative shift of 15 mV occurring over the half-wave potential for Fe/Fe₃C@N-C-1, which is smaller than that of 20 mV for the Pt/C catalyst (Fig. S8d), demonstrating the outstanding ORR stability of the prepared Fe/Fe₃C@N-C-1.

To further verify the ORR pathway on these catalysts, the electron transfer number (n) and H₂O₂% were calculated by Eqs. (3) and (4). The electron transfer number (n) for all three Fe/Fe₃C@N-C catalysts and commercial Pt/C calculated from RRDE measurements were 4.00–4.10 (Fig. S8b), which well agree with the result obtained from the K-L plots. The H₂O₂ yield for Fe/Fe₃C@N-C-1 catalyst was calculated to be less than 3.5% in the measured potential range and dropped to 2.74% at 0.7 V (*vs.* RHE) (Fig. S8c), which is comparable to that of 2.72% for Pt/C (Table S2), indicating that Fe/Fe₃C@N-C-1 is very efficient in catalyzing O₂ into OH⁻ in alkaline electrolytes. The results implied that the Fe/Fe₃C@N-C-1 catalyst is very promising for future applications in ORR-related electrochemical devices.

Based on the structure and the compositional characteristics of Fe/Fe₃C@N-C, the superior electrocatalytic activity of Fe/Fe₃C@N-C-1 towards HER and ORR are mainly ascribed to the following aspects: (1) the porous hierarchical structure accelerate the diffusion of reactants to the surface of catalyst, eventually facilitate the electron transport from the electrode to the reactants molecules [62]; (2) N-doping especially the large proportion of pyridinic N in the hybrid work as active sites and help the formation of active Fe-Nₓ sites [42,44,63]; (3) the Fe and Fe₃C can promote the activity of the Fe-Nₓ sites [14,24,44]; (4) the carbon nanotubes grow on polyhedrons provide more active-sites and act as electron-transfer channels [14]; (5) the carbon shell can enhance the interfacial contact, and suppress Fe and Fe₃C dissolution and agglomeration in the electrolyte, which boost the stability of the electrocatalyst [56]. In view of the above analyses, we propose that the synergetic contributions of the intrinsic active sites (Fe-Nₓ and high proportion of pyridinic N) and the fast electron and ion transport arising from the porous hierarchical structure are mainly responsible for the enhanced electrocatalytic performance.

4. Conclusions

In summary, we have developed a simple strategy for the controlled synthesis of Fe/Fe₃C@N-C hybrids by simply annealing Zn₃[Fe(CN)₆]₂·xH₂O polyhedral particles in nitrogen atmosphere. The Fe/Fe₃C@N-C hybrids show well-defined polyhedron morphology and interesting porous hierarchical structures. It is found that the pyrolysis time plays an important role in the formation of Fe/Fe₃C@N-C hybrids. The Fe/Fe₃C@N-C hybrids can be used as non-noble metal-based electrocatalysts for hydrogen evolution reaction and oxygen reduction reaction. The work will encourage further research on other noble-metal-free catalysts synthesized through the simple and effective metal-organic framework precursor route for renewable energy applications.

Appendix A. Supplementary material

Supplementary data associated with this article can be found, in the online version, at https://doi.org/10.1016/j.jcis.2018.04.026.

References

[1] T.N.J.I. Edison, R. Atchudan, N. Karthik, Y.R. Lee, Int. J. Hydrogen Energy 42 (2017) 14390–14399.
[2] H. Qian, J. Tang, Z.L. Wang, J. Kim, J.H. Kim, S.M. Alshehri, E. Yanmaz, X. Wang, Y. Yamauchi, Chem. Eur. J. 22 (2016) 18259–18264.
[3] Y. Hou, Z.H. Wen, S.M. Cui, S.Q. Ci, S. Mao, J.H. Chen, Adv. Funct. Mater. 25 (2015) 872–882.
[4] Z.Q. Liu, H. Cheng, N. Li, T.Y. Ma, Y.Z. Su, Adv. Mater. 28 (2016) 3777–3784.
[5] A.C. Chen, P. Holt-Hindle, Chem. Rev. 110 (2010) 3767–3804.
[6] E. Antolini, T. Lopes, E.R. Gonzalez, J. Alloys Compd. 461 (2008) 253–262.
[7] J.B. Wu, H. Yang, Acc. Chem. Res. 46 (2013) 1848–1857.
[8] X.X. Zou, Y. Zhang, Chem. Soc. Rev. 44 (2015) 5148–5180.
[9] Z. Schnepp, S.C. Wimbush, M. Antonietti, C. Giordano, Chem. Mater. 22 (2010) 5340–5344.
[10] J.H. Liu, D.D. Zhu, C.X. Guo, A. Vasileff, S.Z. Qiao, Adv. Energy Mater. 7 (2017) 1700518.
[11] F. Jaouen, E. Proietti, M. Lefevre, R. Chenitz, J.P. Dodelet, G. Wu, H.T. Chung, C. M. Johnston, P. Zelenay, Energy Environ. Sci. 4 (2011) 114–130.
[12] C.C. Lv, Z.P. Huang, Q.P. Yang, G.F. Wei, Z.F. Chen, M.G. Humphrey, C. Zhang, J. Mater. Chem. A 5 (2017) 22805–22812.
[13] K.J. Lee, J.H. Lee, S. Jeoung, H.R. Moon, Acc. Chem. Res. 50 (2017) 2684–2692.
[14] A. Aijaz, J. Masa, C. Rosler, H. Antoni, R.A. Fischer, W. Schuhmann, M. Muhler, Chem. Eur. J. 23 (2017) 12125–12130.
[15] Y. Yan, B.Y. Xia, Z.C. Xu, X. Wang, ACS Catal. 4 (2014) 1693–1705.
[16] X.Y. Yu, Y. Feng, B.Y. Guan, X.W. (David)Lou, U. Paik, Energy Environ. Sci. 9 (2016) 1246–1250.
[17] I.E.L. Stephens, A.S. Bondarenko, U. Grønbjerg, J. Rossmeislc, I. Chorkendorff, Energy Environ. Sci. 5 (2012) 6744–6762.
[18] L.B. Ma, Y. Hu, G.Y. Zhu, R.P. Chen, T. Chen, H.L. Lu, Y.R. Wang, J. Liang, H.X. Liu, C.Z. Yan, Z.X. Tie, Z. Jin, J. Liu, Chem. Mater. 28 (2016) 5733–5742.
[19] Y.F. Zhao, X.Q. Xie, J.Q. Zhang, H. Liu, H.J. Ahn, K. Sun, G.X. Wang, Chem. Eur. J. 21 (2015) 15908–15913.
[20] D.Y. Wang, M. Gong, H.L. Chou, C.J. Pan, H.A. Chen, Y.P. Wu, M.C. Lin, M.Y. Guan, J. Yang, C.W. Chen, Y.L. Wang, B.J. Hwang, C.C. Chen, H.J. Dai, J. Am. Chem. Soc. 137 (2015) 1587–1592.
[21] R.J. Zhang, X. Li, L. Zhang, S.Y. Lin, H.W. Zhu, Adv. Sci. 3 (2016) 1600208.
[22] M.K. Debe, Nature 486 (2012) 43–51.
[23] J. Liang, R.F. Zhou, X.M. Chen, Y.H. Tang, S.Z. Qiao, Adv. Mater. 26 (2014) 6074–6079.
[24] Q.C. Wang, Y.P. Lei, Z.Y. Chen, N. Wu, Y.B. Wang, B. Wang, Y.D. Wang, J. Mater. Chem. A 6 (2018) 516–526.
[25] B.Y. Guan, X.Y. Yu, H.B. Wu, X.W. (David) Lou, Adv. Mater. 29 (2017) 1703614.
[26] C.J. Xuan, J. Wang, J. Zhu, D.L. Wang, Acta Phys.-Chim. Sin. 33 (2017) 149–164.
[27] R.R. Salunkhe, Y.V. Kaneti, Y. Yamauchi, ACS Nano 11 (2017) 5293–5308.
[28] S. Dang, Q.L. Zhu, Q. Xu, Nat. Rev. Mater. 3 (2017) 17075.
[29] J.K. Sun, Q. Xu, Energy Environ. Sci. 7 (2014) 2071–2100.
[30] Y.Y. Liu, G.S. Han, X.Y. Zhang, C.C. Xing, C.X. Du, H.Q. Cao, B.J. Li, Nano Res. 10 (2017) 3035–3048.
[31] C. Sanchez, B. Julián, P. Belleville, M. Popallc, J. Mater. Chem. 15 (2005) 3559–3592.
[32] C.M. Doherty, D. Buso, A.J. Hill, S. Furukawa, S. Kitagawa, P. Falcaro, Acc. Chem. Res. 47 (2013) 396–405.
[33] W. Chaikittisilp, K. Ariga, Y. Yamauchi, J. Mater. Chem. A 1 (2013) 14–19.
[34] L.C. He, Y. Liu, J.Z. Liu, Y.S. Xiong, J.Z. Zheng, Y.L. Liu, Z.Y. Tang, Angew. Chem. Int. Ed. 125 (2013) 3829–3833.
[35] S.K. Wu, X.P. Shen, G.X. Zhu, H. Zhou, Z.Y. Ji, L.B. Ma, K.Q. Xu, J. Yang, A.H. Yuan, Carbon 116 (2017) 68–76.
[36] V. Malgras, Q.M. Ji, Y. Kamachi, T. Mori, F. Shieh, K.C.W. Wu, K. Ariga, Y. Yamauchi, Bull. Chem. Soc. Jpn. 88 (2015) 1171–1200.
[37] M.Q. Zhao, X.F. Liu, Q. Zhang, G.L. Tian, J.Q. Huang, W.C. Zhu, F. Wei, ACS Nano 6 (2012) 10759–10769.
[38] X.J. Zheng, J. Deng, N. Wang, D.H. Deng, W.H. Zhang, X.H. Bao, C. Li, Angew Chem. Int. Ed. 53 (2014) 7023–7027.
[39] Q. Li, P. Xu, W. Gao, S.G. Ma, G.Q. Zhang, R.G. Cao, J. Cho, H.L. Wang, G. Wu, Adv. Mater. 26 (2014) 1378–1386.
[40] Q. Li, H.Y. Pan, D. Higgins, R.G. Cao, G.Q. Zhang, H.F. Lv, K.B. Wu, J. Cho, G. Wu, Small 11 (2015) 1443–1452.
[41] L.B. Ma, X.P. Shen, G.X. Zhu, Z.Y. Ji, H. Zhou, Carbon 77 (2014) 255–265.
[42] J.H. Kim, Y.J. Sa, H.Y. Jeong, S.H. Joo, ACS Appl. Mater. Interfaces 9 (2017) 9567–9575.
[43] J.H. Liu, T.K. Zhang, Z.C. Wang, G. Dawsona, W. Chen, J. Mater. Chem. 21 (2011) 14398–14401.
[44] W.J. Jiang, L. Gu, L. Li, Y. Zhang, X. Zhang, L.J. Zhang, J.Q. Wang, J.S. Hu, Z.D. Wei, L.J. Wan, J. Am. Chem. Soc. 138 (2016) 3570–3578.
[45] B.K. Barman, K.K. Nanda, Green Chem. 18 (2016) 427–432.
[46] Y.F. Zhao, J.Q. Zhang, X. Guo, H.B. Fan, W.J. Wu, H. Liu, G.X. Wang, J. Mater. Chem. A 5 (2017) 19672–19679.
[47] Z.H. Wen, S.Q. Ci, F. Zhang, X.L. Feng, S.M. Cui, S. Mao, S.L. Luo, Z. He, J.H. Chen, Adv. Mater. 24 (2012) 1399–1404.
[48] M.B. Wu, Y. Liu, Y.L. Zhu, J. Lin, J.Y. Liu, H. Hu, Y. Wang, Q.S. Zhao, R.Q. Lvc, J.S. Qiu, J. Mater. Chem. A 5 (2017) 11331–11339.
[49] Z.Y. Lu, J. Wang, S.F. Huang, Y.L. Hou, Y.G. Lic, Y.P. Zhao, S.C. Mu, J.J. Zhang, Y.F. Zhao, Nano Energy 42 (2017) 334–340.
[50] L.B. Ma, X.P. Shen, J. Zhu, G.X. Zhu, Z.Y. Ji, J. Mater. Chem. A 3 (2015) 11066–11073.
[51] I. Vlassiouk, M. Regmi, P. Fulvio, S. Dai, P. Datskos, G. Eres, S. Smirnov, ACS Nano 5 (2011) 6069–6076.
[52] Y.Y. Hao, M.S. Bharathi, L. Wang, Y.Y. Liu, H. Chen, S. Nie, X.H. Wang, H. Chou, C. Tan, B. Fallahazad, H. Ramanarayan, C.W. Magnuson, E. Tutuc, B.I. Yakobson, K. F. McCarty, Y.W. Zhang, P. Kim, J. Hone, L. Colombo, R.S. Ruoff, Science 342 (2013) 720–723.
[53] Z. Yan, J. Lin, Z.W. Peng, Z.Z. Sun, Y. Zhu, L. Li, C.S. Xiang, E.L. Samuel, C. Kittrell, J.M. Tour, ACS Nano 6 (2012) 9110–9117.
[54] H.J. Zhang, H. Li, X. Li, H. Qiu, X. Yuan, B. Zhao, Z.F. Ma, J.H. Yang, Int. J. Hydrogen Energy 39 (2014) 267–276.
[55] Z.Y. Liu, G.X. Zhang, Z.Y. Lu, X.Y. Jin, Z. Chang, X.M. Sun, Nano Res. 6 (2013) 293–301.
[56] Y.Y. Liu, H.T. Wang, D.C. Lin, J. Zhao, C. Liu, J. Cui, Nano Res. 10 (2017) 1213–1222.
[57] W.F. Chen, J.T. Mucherman, E. Fujita, Chem. Commun. 49 (2013) 8896–8909.
[58] M.H. Shao, Q.W. Chang, J.P. Dodelet, R. Chenitz, Chem. Rev. 116 (2016) 3594–3657.
[59] J. Lu, W.J. Zhou, L.K. Wang, J. Jia, Y.T. Ke, L.J. Yang, K. Zhou, X.J. Liu, Z.H. Tang, L. G. Li, S.W. Chen, ACS Catal. 6 (2016) 1045–1053.
[60] J.Y. Liu, Y. Liu, P. Li, L.H. Wang, H.R. Zhang, H. Liu, J.L. Liu, Y.X. Wang, W. Tian, X. B. Wang, Z.T. Li, M.B. Wu, Carbon 126 (2018) 1–8.
[61] L. Sun, Y. Luo, M. Li, G.H. Hu, Y.J. Xu, T. Tang, J.F. Wen, X.Y. Li, L. Wang, J. Colloid Interface Sci. 508 (2017) 154–158.
[62] M.T. Liu, L.X. Chen, A.J. Wang, K.M. Fang, J.J. Feng, Int. J. Hydrogen Energy 42 (2017) 25277–25284.
[63] K. Yuan, S. Sfaelou, M. Qiu, D.L. Hecht, X.D. Zhuang, Y.W. Chen, C. Yuan, X.L. Feng, U. Scherf, ACS Energy Lett. 3 (2018) 252–260.